**Proceedings of ASME Turbo Expo 2011**
**GT2011**
**June 6-10, 2011, Vancouver, British Columbia, Canada**

**GT2011-45915**

# MASSIVELY-PARALLEL DNS AND LES OF TURBINE VANE ENDWALL HORSESHOE VORTEX DYNAMICS AND HEAT TRANSFER

**Markus Schwänen, Michael Meador, Josh Camp, Shriram Jagannathan, Andrew Duggleby***
Department of Mechanical Engineering
Texas A&M University
College Station, Texas 77843
Email: aduggleby@tamu.edu

## ABSTRACT

*Higher turbine inlet temperatures enable increased gas turbine efficiency but significantly reduce component lifetimes through melting of the blade and endwall surfaces. This melting is exacerbated by the horseshoe vortex that forms as the boundary layer stagnates in front of the blade, driving hot gasses to the surface. Furthermore, this vortex exhibits significant dynamical motions that increase the surface heat transfer above that of a stationary vortex. To further understand this heat transfer augmentation, the dynamics of the horseshoe vortex must be characterized in a 3D time-resolved fashion which is difficult to obtain experimentally. In this paper, a 1st stage high pressure stator passage is examined using a spectral element direct numerical simulation at a Reynolds number* $Re = U_\infty C/\nu = 10,000$*. Although the Re is lower than engine conditions, the vortex already exhibits similar strong aperiodic motions and any uncertainty due to sub-grid scale modeling is avoided. The vortex dynamics are analyzed and their impact on the surface heat transfer is characterized. Results from a baseline case with a smooth endwall are also compared to a passage with film cooling holes. Higher Reynolds number simulations require a Large Eddy Simulation turbulent viscosity model that can handle the high accelerations around the blade. A high-pass-filter sub-grid scale model is tested at the same low Reynolds number to test its effectiveness by direct comparisons to the DNS. This resulted in a significant drop in turbulence intensity due to the high strain rate in the freestream, resulting in different dynamics of the vortex than observed in the DNS. Appropriate upstream engine conditions of high freestream turbulence and large integral length scales for all cases are generated via a novel inflow turbulence development domain using a periodic solution of Taylor vortices that are convected over a square grid. The size of the vortices and grid spacing is used to control the integral length scale, and the intensity of the vortices and upstream distance is used to control the turbulence intensity. The baseline DNS exhibits a bi-modal horseshoe vortex, and the presence of cooling-holes qualitatively increases the number of vortex cores resulting in more complex interactions.*

## NOMENCLATURE

| | |
|---|---|
| $C_{ax}$ | Axial Chord |
| $C$ | Chord |
| $C_s$ | Smagorinsky constant (LES model) |
| $D$ | Hemisphere diameter (LES validation) |
| $DNS$ | Direct Numerical Simulation |
| $FSTI$ | Freestream Turbulence Intensity |
| $GLL$ | Gauss-Lobatto-Legendre |
| $H_{12}$ | Form factor |
| $HPF$ | High Pass Filter |
| $LES$ | Large Eddy Simulation |
| $Re$ | Reynolds number |
| $P$ | Pressure |
| $S$ | Blade Span |
| $S_{ij}$ | Strain tensor |
| $St$ | Stanton number $St = \frac{h}{\rho C_p U_\infty}$ |
| $TI$ | Turbulence Intensity |

*Address all correspondence to this author.

| | |
|---|---|
| $U_\infty$ | Freestream velocity |
| $U_e$ | Boundary layer edge velocity |
| $X,Y,Z$ | Streamwise, pitchwise and spanwise coordinate |
| $u_i = (u,v,w)$ | Velocity vector |
| $\Delta$ | Filter Width |
| $\Lambda$ | Integral length scale |
| $\Psi$ | Streamfunction |
| $\alpha$ | Thermal diffusivity |
| $\delta_1$ | Displacement thickness of a boundary layer |
| $\delta_2$ | Momentum thickness of a boundary layer |
| $\delta_{ij}$ | Kronecker delta |
| $\lambda$ | Eigenvalue for Walsh solution |
| $\nu$ | Kinematic viscosity |
| $\nu_t$ | Eddy viscosity |

## 1 Introduction

Direct Numerical Simulations (DNS) and Large Eddy Simulations (LES) offer high data-density of three-dimensional and time-dependent velocity and temperature fields, often in greater detail (both space and time) than can be experimentally obtained. Once simulation confidence is achieved and data validated with experiments, this data can be analyzed through advanced techniques to observe structures, interactions, and correlations, ultimately elucidating the complex flow physics. This advanced knowledge of the physics then allows for the development of new optimized systems and geometries, playing a key role in solving engineering challenges.

This is especially true in the realm of gas turbine endwall cooling where the stagnating boundary-layer vortex, depicted in Fig. 1 (top) from Langston (2001) [1] undergoes significant unsteady spatial oscillations in the midst of high free stream fluctuations. This vortex motion is responsible for a large amount of drag and heat transfer that results in thermal failure (melting) shown in Fig. 1 (bottom) from Thole (2008) [2]. While endwall contouring shows promise in reducing this effect [3, 4], there remains large efficiency gains that can only be discovered by knowing more about the underlying physics via supercomputing simulations and novel analysis techniques [5].

The stagnating boundary-layer vortex flow was first studied in relation to turbomachinery by Gaugler & Russell (1984) [6] who examined the boundary-layer vortex effects in a time varying manner. They identified, through flow visualization and surface heat transfer, that high convective heat transfer coefficients coincided with the most intense vortex action. While the importance of this vortex in heat transfer is recognized, there are only a few scarce three-dimensional flow field measurements that have been made to understand its dynamics and sensitivity to system design.

In the stagnation region of a first stage turbine stator vane, Laser Doppler Velocimetry measurements were performed by Kang et al. (1999) [7]. They showed through flow field and heat

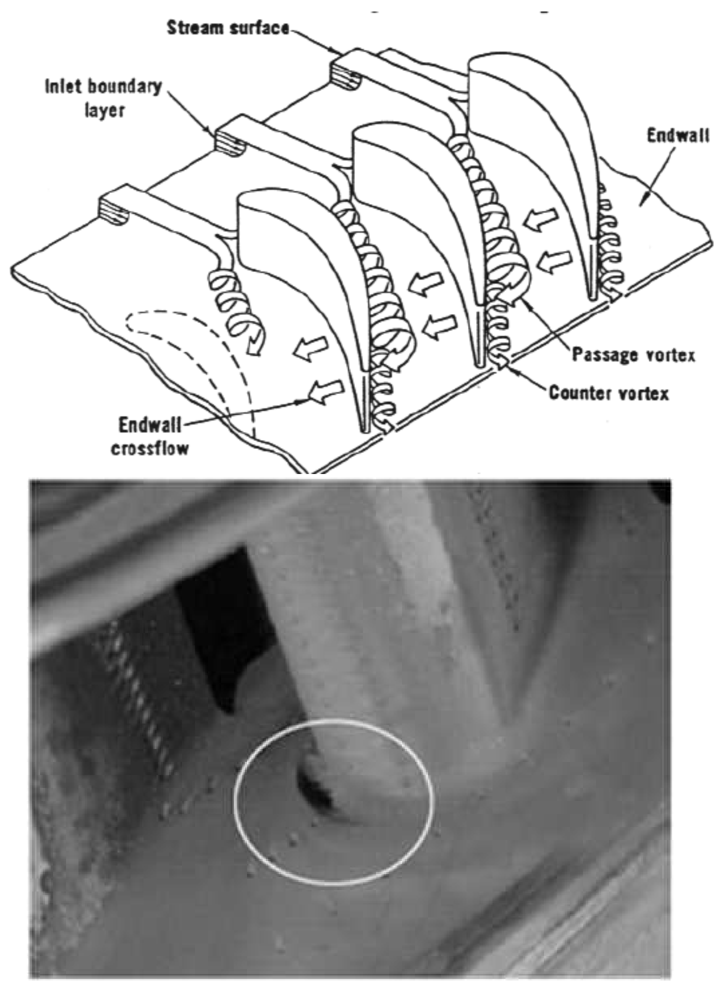


**FIGURE 1**. Horseshoe vortex rolls up from the stagnating boundary, depicted by Langston (2001) [1] (top). Melting occurs when the horseshoe vortex drives hot combustion gasses to the surface (bottom, from Thole (2008) [2]).

transfer measurements that the peak heat transfer downstream coincided with the downward flow associated with the vortex. This brings hot, high-speed freestream fluid towards the endwall, thins the boundary layer, and ultimately increases the local heat transfer causing a quick rise in component surface temperature. Contours of turbulent kinetic energy reveal a peak that coincides with the horseshoe vortex center. Likewise, the profile peaks of root-mean-square (rms) velocities coincide closely with the vortex center. Only the peak streamwise fluctuations occurring slightly upstream of the vortex center. Comparing this to canonical turbulent boundary layer flows, where the peak is less than 15%, it is evident that the horseshoe vortex causes the higher fluctuations. This is in agreement with the data previously presented by Devenport & Simpson (1980) [8] who also reported very high turbulent kinetic energy levels in the vortex region.

It is believed that the unsteady motion of the horseshoe vortex accounts for the increased local turbulence. Histograms of the velocity probability density functions (PDF) from Radomsky et al. (2000) [9] indicate a more standard turbulent Gaussian distribution exists far above the endwall. Closer towards the endwall near the vortex center, the velocity PDF shows two distinct peaks with a shift in the relative heights of the peaks. These two peaks indicate that the flow is oscillating, or rather unsteady, in the vortex region. The unsteadiness of the horseshoe vortex, amplification of free stream turbulence, and wall generated turbulence cause high turbulence intensities in the leading edge vortex [9]. The vortex motion in combination with the high turbulent intensities at the combustor exit, ranging from 8% to 40%, greatly enhances endwall heat transfer [9].

Furthermore, upstream flow features appear to complicate the vortex dynamics. Endwall heat transfer with cooling holes, examined by Knost et al. (2008) [10], explored the leakage bypass flow from the combustor-turbine endwall. Although the purpose of the study was to evaluate a three dimensional sinusoidal slot, it was observed that only the sinusoid phase angle produced any significant change in coolant. Different waveform amplitudes and centerline locations did not provide any significant effect to the region dominated by the horseshoe vortex. Regarding upstream turbulence effects on secondary losses, Gregory-Smith et al. [11] showed that the secondary losses are not greatly affected by high freestream turbulence and a significant part of the losses are due to anisotropic Reynolds Stresses that a standard RANS solver cannot capture. Spencer and Jones et al. [12] reported endwall heat transfer measurements using a transient liquid crystal technique in annular cascades of nozzle guide vanes. In their geometry, the horseshoe vortex separates early and thus does not augment the heat transfer near the endwall hub.

In summary, the current knowledge of the horseshoe vortex dynamics and its effect on endwall heat transfer is inadequate without large scale computational results and 3D time dependent experimental data. Towards that goal, this paper presents 1st stage stator vane and endwall direct numerical simulations (with and without cooling holes), examining the structures and dynamics of the dominant horseshoe vortex and characterize its effect on endwall heat transfer. Also presented is the benchmarking of a large eddy simulation (without cooling holes), comparing it to the DNS to test the capability of a high-pass-filter based Smagorinsky model for use in turbomachinery.

## 2 Numerical Method

To examine the horseshoe vortex and its effect on endwall heat transfer, a single blade in the cascade with periodic boundary condition in the pitchwise direction is considered, with the same geometry from Knost el al. (2008) [10], Knost and Thole (2005a) [13], and Knost and Thole (2005b) [14]. As endwall heat transfer is only mildly a function of Mach number, the current and previous simulations [10, 13], as well as experiments [14], are incompressible. The bottom spanwise boundary is treated as a no-slip wall. The domain extends 0.75 chord lengths ($C$) downstream ($X$ direction) of the trailing edge and about 4.60 $C$ upstream of the blade stagnation (this includes the turbulence generating section). The domain height is equal to half the blade span, where a slip condition (stress free) is applied at the top. The Reynolds number for all cases is Re = $U_\infty C/\nu$= 10,000. Three cases are considered in this investigation:

1. DNS without cooling holes.
2. DNS with cooling holes.
3. LES without cooling holes
   (used for testing the HPF Smagorinsky model).

Although the Reynolds number is lower than engine conditions, the vortex already exhibits similar strong, aperiodic motions, and any uncertainty due to sub-grid scale modeling is avoided in the DNS. This also provides a testbed for examining appropriate LES models that can handle the high free-stream turbulence and strong accelerations around the blade.

The algorithm used to solve the flow is NEK5000, a spectral element solver developed over the last 20 years for turbulence research [15–22]. NEK5000 solves the Navier-Stokes equations which represent conservation of mass, momentum, and energy

$$\frac{\partial u_j}{\partial x_j} = 0, \tag{1}$$

$$\left(\frac{\partial}{\partial t} + u_j\frac{\partial}{\partial x_j}\right)u_i = -\frac{1}{\rho}\frac{\partial}{\partial x_i}P + \nu\frac{\partial^2}{\partial x_j \partial x_j}u_i + \frac{\partial \tau_{ij}^{SGS}}{\partial x_j}, \tag{2}$$

$$\left(\frac{\partial}{\partial t} + u_j\frac{\partial}{\partial x_j}\right)T = \alpha\frac{\partial^2}{\partial x_j \partial x_j}T, \tag{3}$$

with velocity $u_i$, pressure $P$, temperature $T$, kinematic viscosity $\nu$, thermal diffusivity $\alpha$, and for LES the subgrid stress tensor $\tau_{ij}$. Only the DNS simulations presented in this paper included temperature with a Prandtl number of Pr=$\nu/\alpha$ = 0.71. NEK5000 employs a geometrically flexible yet exponentially convergent spectral element discretization in space, dividing the computation into elements over which the solution is represented as a high-order (usually 11-13) Lagrangian interpolant. This data localization allows for minimal communication between elements resulting in efficient parallelization. Currently the solver has shown sustained performance for over 230,000 processors with 70% parallel efficiency [23]. Time discretization is done with high-order operator splitting methods, and Tensor-product polynomial bases are solved using conjugate gradient iteration with scalable Jacobi and hybrid Schwarz/Multigrid preconditioner [17].

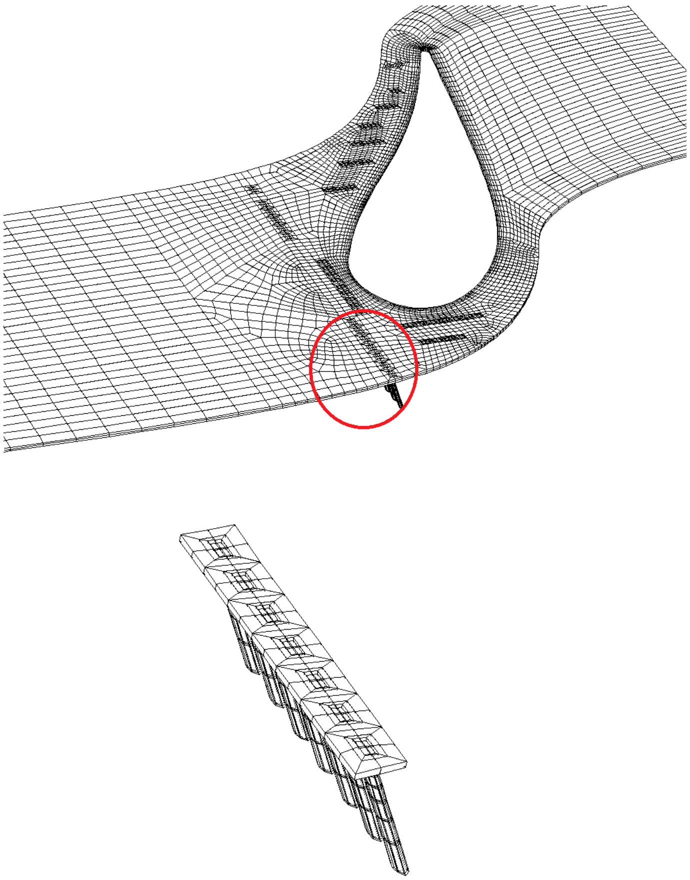

**FIGURE 2**. Element structure on the endwall (top - shown at a low polynomial order). A closeup of the cooling holes (red-circle) is also shown (bottom). There are 49 cooling holes in this domain in the same configuration as Knost et al. [10]. The domain consists of 150,016 elements. At a polynomial order of 6, the simulation has 32.4 Million grid points. Coarsening above the cooling holes (bottom) yields a reduction in the total element count by 25k elements.

### 2.1 Grid Generation

NEK5000 requires that the domain be meshed with high quality, structured, hexahedral elements. For complicated geometries, such as the present domain, a great deal of planning and creativity is needed in order to not only produce a quality hexahedral mesh, but to also keep the total element count low while still ensuring that key locations in the domain are highly resolved. In particular, the cooling holes present at the endwall provide a significant challenge in producing a production-quality mesh.

The domain has too many complex features (curved blade, cooling holes) for the standard NEK5000 meshing utility to handle. Therefore Gambit 2.4.6 is used to generate the mesh, shown in Fig. 2. However, a standard Gambit mesh does not necessarily work in spectral elements. Furthermore, Gambit does not output in a format compatible with NEK5000 or identify periodic faces in a manner suitable for NEK5000. The mesh is exported in an ASCII-format neutral file, which is then converted to a NEK5000-compatible format by way of an in-house code. Within this code, all the interfacing steps necessary for spectral elements use are implemented.

Also, a challenging step using structured spectral elements is to provide appropriate coarsening away from the boundary layer and away from the cooling holes to avoid unnecessarily high element counts. The current strategy involves coarsening structures around the endwall cooling holes exits, boundary layer conforming meshes near the blade surface and the endwall, and strategic use of alternative face meshing algorithms. The cooling hole exits present on the end wall require a higher resolution in order to accurately follow the geometry, as well as to capture the flow behavior present. However, the relatively higher resolution is only needed near the wall. In order to allow the mesh to naturally coarsen away from the endwall, a boxing structure is used so that a portion of the finer mesh of the cooling hole exit is self-contained. For the present domain, a significant savings on total element count was achieved by using this method. In the present study, use of the boxing structure on each of the 49 holes resulted in reducing the final element count by 25,284 elements. Fig. 3 shows a simple 2D example demonstrating the reduction in resolution from using the boxing structure.

Efficient use of a boundary layer meshing near no-slip boundaries allows a simulation to capture the pertinent effects of boundary layer growth while allowing for coarsening to occur far away from the wall. This domain uses boundary layer meshes near both the endwall and the vane. Knost et al. (2008) [10] determined that the wall shear stress is highest at the leading edge of the vane. This shear stress is used to predict the boundary layer height to ensure that the boundary layer effects are captured in the boundary layer mesh. As a conservative approach, these boundary layer parameters are also employed on the endwall boundary layer mesh.

Finally, the amount of cooling holes (and subsequently, cooling hole meshes) requires that a more efficient meshing algorithm than simple mapping be used. Use of both the Tri-Primitive and PAVE [24] meshing schemes allows for the mesh to be coarsened along the endwall away from the cooling holes, effectively reducing the total number of elements in the domain. Most importantly, use of higher complexity meshing algorithms allows the periodic faces in the domain to be truly periodic, matching both element shape and Gauss-Lobatto point positions.

The mesh consists of 150,016 elements. At polynomial order of 5, the cooling-hole simulation is comprised of 18.8 Million grid points. The non-cooling hole mesh comprised of 94,032 elements at 7th order for 32.2 Million grid points. Although the above listed meshing strategies are standard for finite element

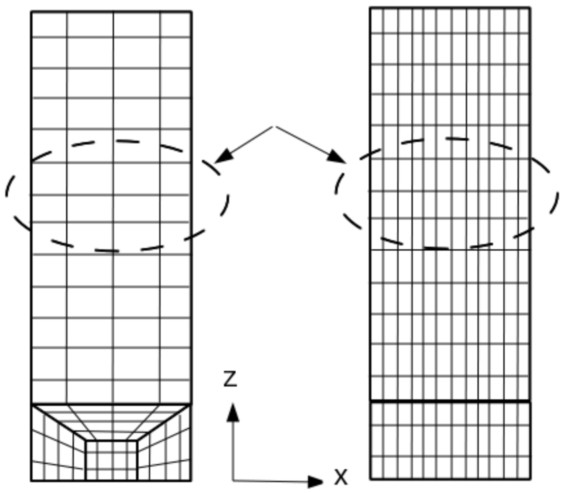


**FIGURE 3**. Example 2D coarsening structure (left) made available through Gambit compared to a similar mesh with no coarsening using NEK5000 mesh generation (right). A portion of the mesh on the bottom edge is self-contained inside the box, allowing coarsening to occur naturally. The z-axis is in the wall normal direction. The circled portions highlight the magnitude of coarsening. In this example, the element count is reduced by 45.8% (104 elements to 192 elements) by interfacing Gambit with NEK5000 instead of using the NEK5000 meshing tool.

or finite volume simulations, these simulations represent one of the most complex geometry spectral element simulations in open literature.

## 2.2 Numerical Domain and Boundary Conditions

The flow domain for the 1st stage stator vane is shown in Fig. 4. A nearly isotropic turbulence is generated by allowing a divergence free velocity field with multiple vortices at the inflow plane, $X/C = -4.6$, to advect inside a doubly periodic (in $Y$ and $Z$) box until $X/C = -4.2$. An array of bars then initiate the redistribution of turbulent kinetic energy downstream and turbulence is allowed to decay untill the cascade. The rate of decay depends on the distance between the grid and the cascade inlet, which can be changed at run-time by scaling the domain in the $X$-direction. The streamfunction of the velocity field at the inlet is given by:

$$\psi = \frac{1}{4}\cos(3z)\sin(4y) - \frac{1}{5}\cos(5y) - \frac{1}{5}\sin(5z), \quad (4)$$

$$-\nabla^2\psi = \lambda\psi, \quad (5)$$

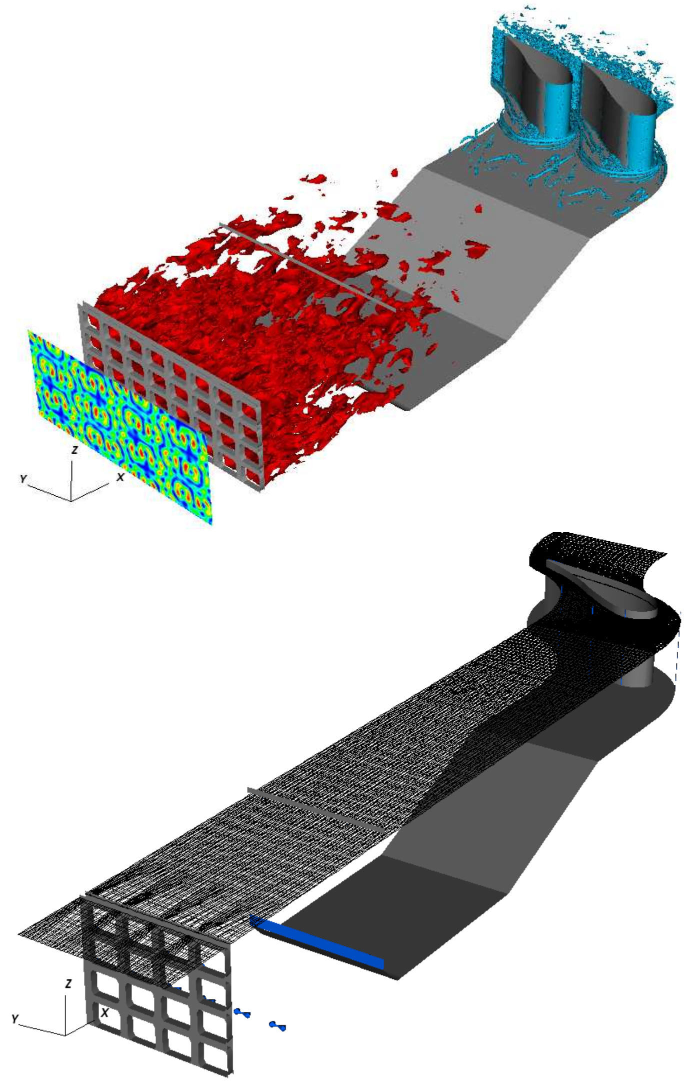


**FIGURE 4**. Flow domain for a high pressure turbine vane, shown with the domain doubled for clarity. Blade geometry matches Knost et al. (2008) [10], with periodic conditions. (Top) Upstream is the Walsh solution which convects over the blade. Shown are contours of velocity magnitude. Downstream blue isocontours of vorticity shows the dynamics of the horseshoe vortex. (Bottom) Grid and domain boundaries. Blue indicates the rearward facing step where mass is removed to control boundary layer thickness. These simulations represent one of the most complex geometry spectral element simulations in open literature.

where $\psi$ is the streamfunction and $\lambda$ is the Eigenvalue of the Laplacian. This allows parametric control of freestream turbulence intensity and length scales by varying the amplitude and wavenumbers of the sine and cosine functions, respectively. Increasing the wavenumbers result in smaller vortices at the inflow plane. The average size of these eddies controls the length scale' as long as it is smaller than the open grid area.

To counteract the dissipation of turbulent kinetic energy in the inflow generating section, the Reynolds number is artificially increased in a region extending downstream of the grid bars to the middle of the ramp. This decreases the impact of viscosity on the momentum balance and effectively increasing Reynolds number. To prevent reverse flow at outflow boundaries, a source term in the divergence equation (conservation of mass) is added in the last row of elements which causes the flow to accelerate out. This helps quickly advect out any large vortices that otherwise cause reverse flow issues.

In order to refine the mesh near the walls in the main passage with a structured mesh, a small backward facing step is connected to the periodic box. However, preliminary simulations indicated that the homogeneity of flow is affected by the low momentum fluid that is formed in the recirculation region. This fluid could entrain into the main flow affecting the homogeneity of flow. Thus, the backward facing step is made porous and sucks fluid out of the domain opposite to the streamwise direction. This deflects the flow towards the endwall and reduces the reattachment length without affecting the flow away from wall. This loss of flow rate is accounted for while setting the Reynolds number based on freestream velocity. A ramp downstream of the step (extending from $X/C = -2$ to $X/C = -1$) controls the development of the boundary layer and also creates a favorable pressure gradient that is dependent on its slope.

### 2.3 LES High-Pass-Filtered Smagorinsky Model

To ultimately reach engine conditions, an LES with an appropriate sub-grid scale (SGS) model is essential to provide sufficient dissipation in under-resolved regions of flow and to account for interaction between sub-grid scale and large scales. A significant challenge, however, is finding an SGS model that can handle the high anisotropy, separation, and sometimes relaminarization that can occur in turbomachinery flows. One model that appears to have the ability to meet these requirements is a high-pass filtered Smagorinsky model developed by Stolz et al. [25]. Since the model is based on HPF velocity strain-rate the eddy viscosity vanishes in laminar flow regimes which is essential in transitional flows. Secondly, a reduced eddy viscosity is predicted near the walls which eliminates the need to use near-wall damping functions. The model employs high-pass filtered quantities for calculating eddy viscosity and strain rate:

$$\tau_{ij}^{SGS} - \frac{\delta_{ij}}{3}\tau_{kk}^{SGS} = -2\nu_t^{HPF} S_{ij}, \tag{6}$$

$$S_{ij} = \frac{1}{2}\left(\frac{\partial u_i}{\partial x_j} + \frac{\partial u_j}{\partial x_i}\right), \tag{7}$$

$$\nu_t^{HPF} = \left(C_s^{HPF}\Delta\right)^2 \mid S_{ij}(\tilde{u}) \mid, \tag{8}$$

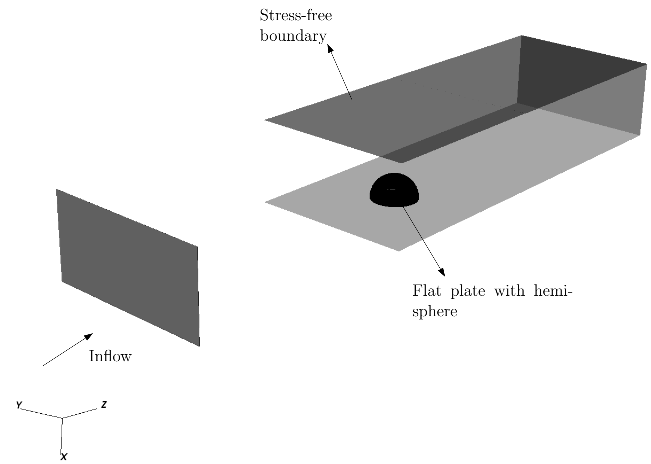


**FIGURE 5**. Flow over a flat plate with hemisphere for testing the High Pass Filtered Smagorinsky model. The figure shows the non-periodic faces in the domain. The freestream turbulence is generated by a recycling and rescaling technique by choosing a recycling plane downstream of the inflow plane. The velocities at the recycling plane are scaled and copied to the inflow plane to match the chosen turbulence intensity inside the box.

where $\Delta$ is the filter width taken as the largest distance between the Gauss-Lobatto-Legendre (GLL) points in physical space, $C_s^{HPF}$ is a constant with a value 0.1, and $\tilde{u}$ is the high pass filtered velocity field. A dynamic version of the model with varying $C_s^{HPF}$ is possible; however, the fixed co-efficient has shown satisfactory results in Stolz [25] and is thus chosen for the present investigation.

The model was tested and appropriate high-pass-filter transfer function was found by setting up a turbulent flow over a flat plate with a hemispherical protuberance. The results are validated against a DNS at the same Reynolds number. The flow domain shown in Fig. 5. Nearly isotropic turbulence is generated by a recycling and rescaling method introduced by Stolz et al. [26]. At a certain distance downstream of the inflow plane, a recycling plane is chosen. The mean velocities are scaled such that the volume averaged velocity inside the box is one and then copied back to the inflow plane. The inflow and recycling planes are located at $Z/D = -5.0$ and $Z/D = -0.22$. The turbulent intensity (TI) inside the recycling domain is maintained by implementing a simple Proportional-Integral-Derivative (PID) controller. At each time step, the spatial intensity in the recycling box is compared to a desired value. If too low, additional vortices are added by combining a percentage of Eqn. 4 with the copied recycling plane flow. If the intensity is too high, no vortices are added and the viscosity naturally dampens the intensity.

At $Z/D = 0$, a flat plate initiates the formation of boundary

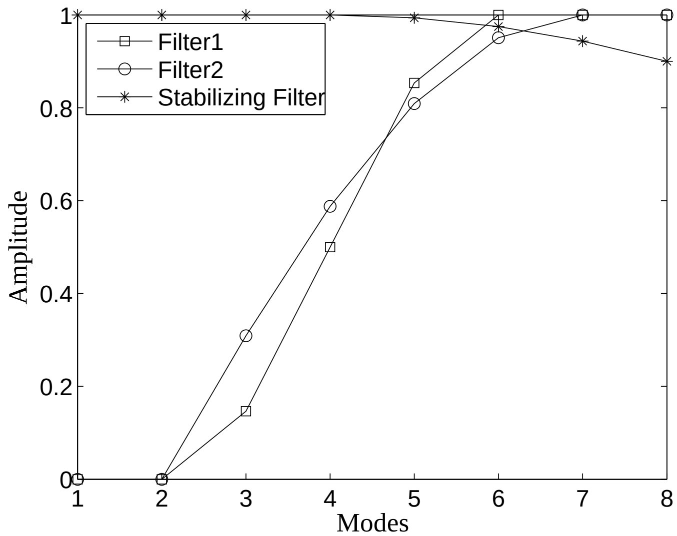


**FIGURE 6**. The filter transfer functions are set similar to a cosine function that filters the large scales and leaves the small scales unfiltered. A stabilizing filter is used for all simulations (DNS and LES) where the last 4 modes are filtered with a weight of 0.10.

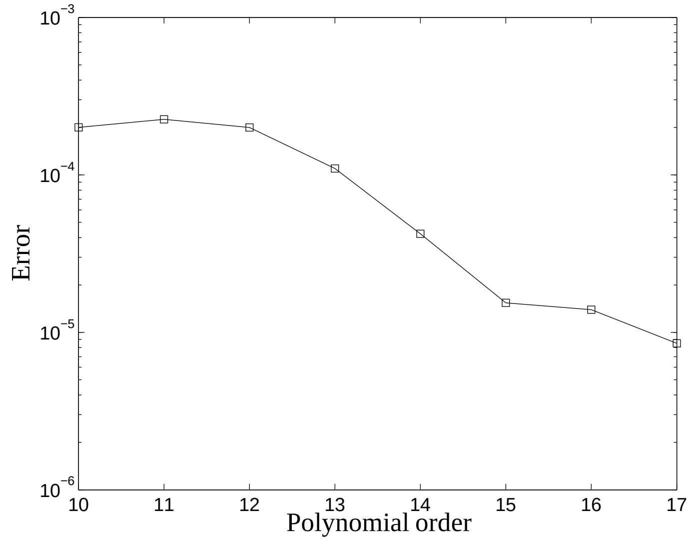


**FIGURE 7**. A fairly constant slope on a semi-log plot of error vs polynomial order signifies an exponential convergence for the hemisphere DNS. Data is acquired at a polynomial order of 14.

layer upstream of the hemisphere that is located at $Z/D = 2.0$. A stress free boundary condition is used in the pitchwise direction for the non-recycling domain. The streamwise velocity and rms profiles at different downstream locations of the hemisphere are considered for comparison against the DNS. The two different filter functions tested are shown in Fig. 6. Additionally, a stabilizing filter developed by Fischer et al. [27] is used for the spectral element basis function that filters out the high frequency components shown in Fig. 6. The filter is applied after each time step and also preserves inter-element continuity [28]. This avoids the non-physical spectral build up in the energy spectra that is usually found in under-resolved DNS or LES. The HPF Smagorinsky model is applied after each time step and acts upon the velocity components filtered by the stabilizing filter. A convergence study for the DNS is reported in Fig. 7. This shows exponential convergence typical of spectral methods, and that a polynomial order 14 is sufficient for the DNS.

Time-averaged mid-section velocity profiles at $0.5D, 1.5D, 2.5D$ downstream of the hemisphere are shown in Fig. 8. The velocity profiles are in reasonable agreement except at $2.5D$ where Filter1 performs better near the boundary layer and is thus chosen for production runs. The corresponding rms velocity profile for Filter1 is shown in Fig. 9. While there are few discrepancies between the LES and DNS rms profiles, the LES follows the trend predicted by the DNS in most flow regimes.

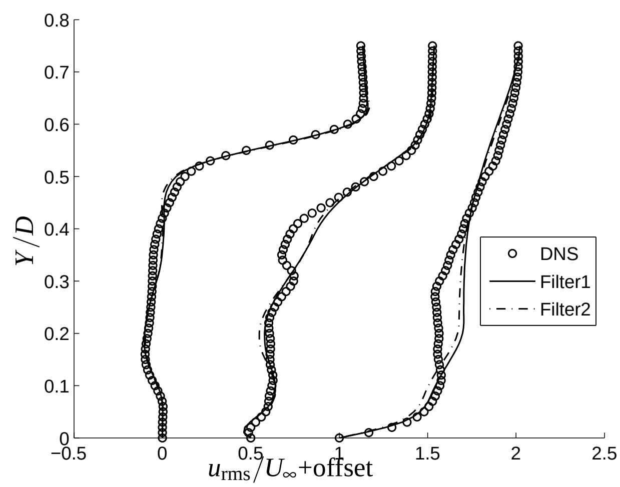


**FIGURE 8**. Streamwise velocity profiles at $0.5D, 1.5D, 2.5D$ downstream of the hemisphere, offset by 0.5, respectively. The profiles are in good agreement with the DNS, except at$2.5D$ where Filter1 performs better predicting the boundary layer growth in accordance with the DNS.

## 3 Results and Discussions

A DNS and LES of a first stage stator is performed using NEK5000. As reported earlier, the mesh consisted of 94,032 elements with polynomial order 7 for the non-cooling hole case DNS and poly order 5 for the LES. For the cooling hole case 150,016 elements with polynomial order 5 for the cooling hole

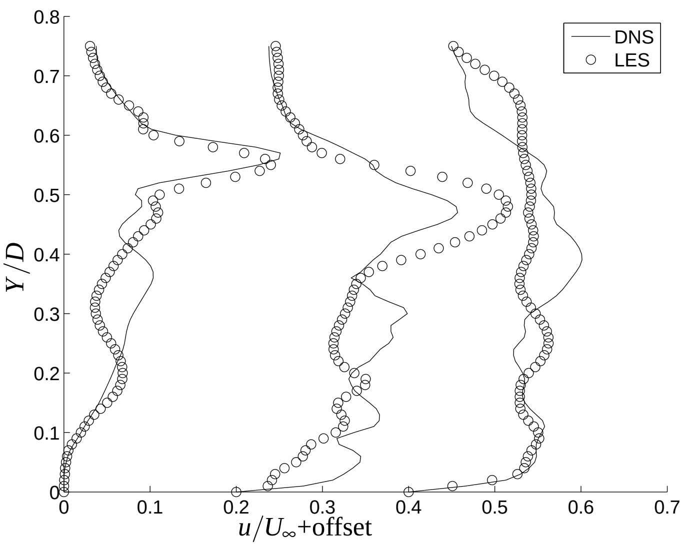


**FIGURE 9**. Streamwise fluctuation velocity profiles at $0.5D, 1.5D, 2.5D$ downstream of the hemisphere, offset by 0.2, respectively. The filtered rms profiles are in fair agreement following the trend predicted by the DNS.

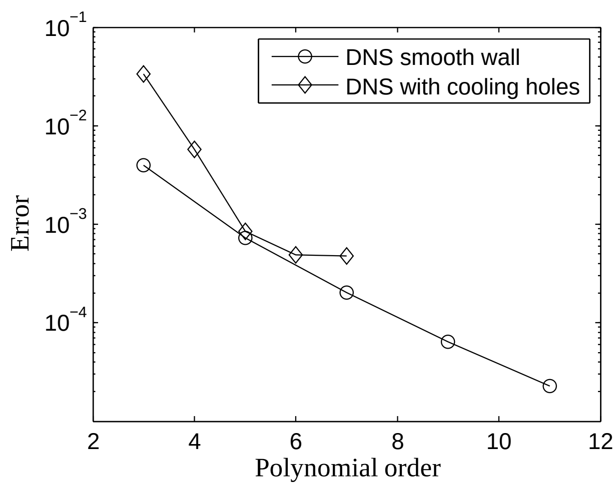


**FIGURE 10**. A fairly constant slope on a semi-log plot of error vs polynomial order signifies an exponential convergence for the turbine DNS cases. Data is acquired at a polynomial order of 7 for the non-cooling hole and 5 for the cooling hole case.

case are used. The number of elements, polynomial order, and CPU time are reported in Table 1. The convergences for the DNS cases are shown in Fig. 10.

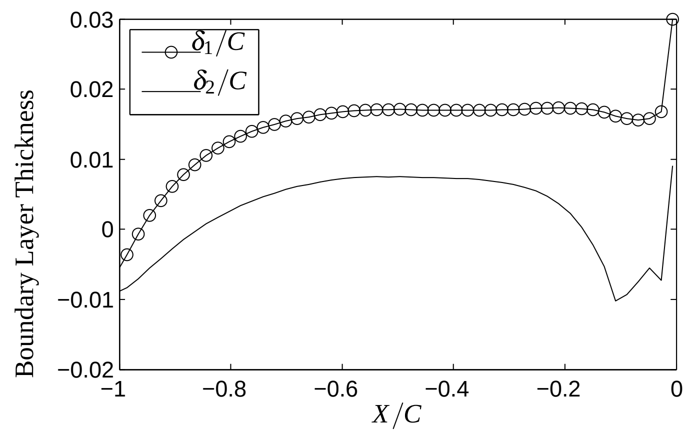


**FIGURE 11**. Displacement and momentum thickness on $Y/P = 0$ approaching the vane. The displacement thickness normalized with chord at $X/C = -1/3$ is 0.0170 for the DNS vs. 0.0146 (at 20% TI) from Radomsky et al. [9].

**TABLE 1**. Number of elements, polynomial order, total grid points, and total CPU hours for the DNS with no cooling holes (DNS1), DNS with cooling holes (DNS2) and the LES (without cooling holes). Simulations were performed on 1024 processors (TAMU Supercomputing Center, EoS and NSF Teragrid, Kraken).

| Case | # Elements | Poly order | Grid pts | CPU hrs |
|---|---|---|---|---|
| DNS1 | 94,032 | 7 | $32.2\times10^6$ | 44,000 |
| DNS2 | 150,016 | 5 | $18.8\times10^6$ | 113,000 |
| LES | 94,032 | 5 | $11.8\times10^6$ | 20,000 |

### 3.1 Inflow characteristics

To properly simulate flow and heat transfer in a first stage stator vane, the incoming flow needs to have features that are characteristic of the flow exiting a combustion chamber. The simulation inlet and geometry is adjusted to match parameters described in Radomsky et al. (2000) [9] and Knost et al. (2008) [10]. While the displacement thickness shown in Fig. 11 compares favorably, the integral length scale is a little lower and the turbulence intensity compares well to the lowest turbulence intensity experimental case. The profiles in the pitch-wise direction of those quantities are fairly homogeneous. From Fig. 12, it can be seen that the velocity profile has a slight overshoot close to the wall downstream of the converging section. But as the flow approaches the vane ($X/C > -1/3$), the boundary layer develops a fairly constant free stream mean velocity profile.

Fig. 13 shows the decay of fluctuating streamwise velocity from the grid to the cascade at half the domain height (1/4 span). The TI decay is exponential and turbulence is nearly isotropic just before the cascade ($X/C = -1/3$). Using the methods de-

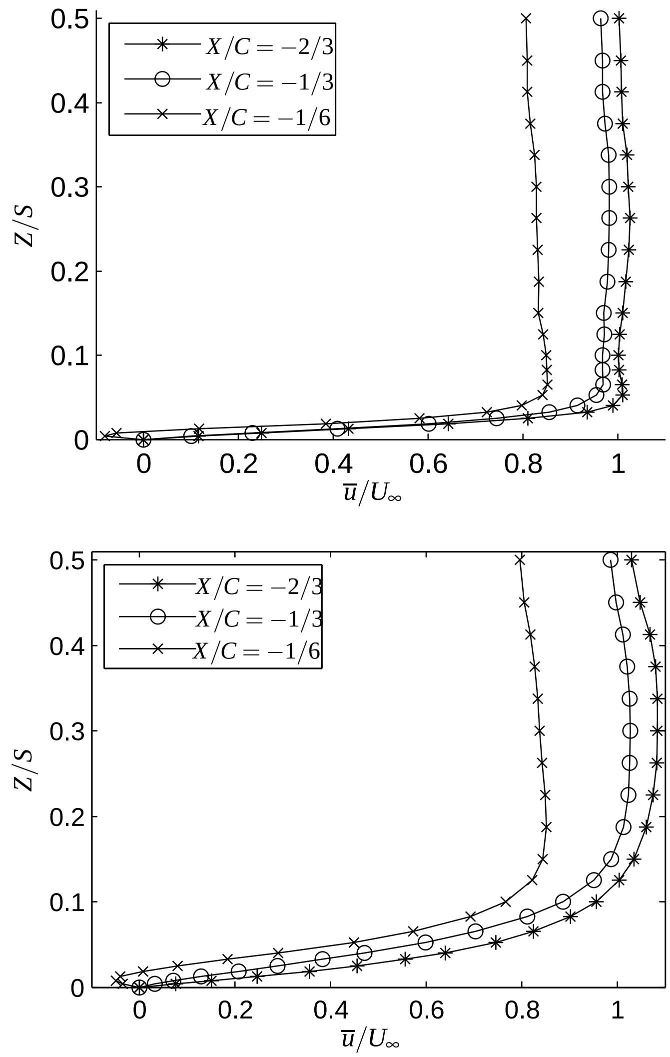


**FIGURE 12**. Time-averaged boundary layer profiles scaled with outer variables at different streamwise locations are shown for the DNS (top) and LES (bottom). The profile closest to the vane is already influenced by the stagnation pressure.

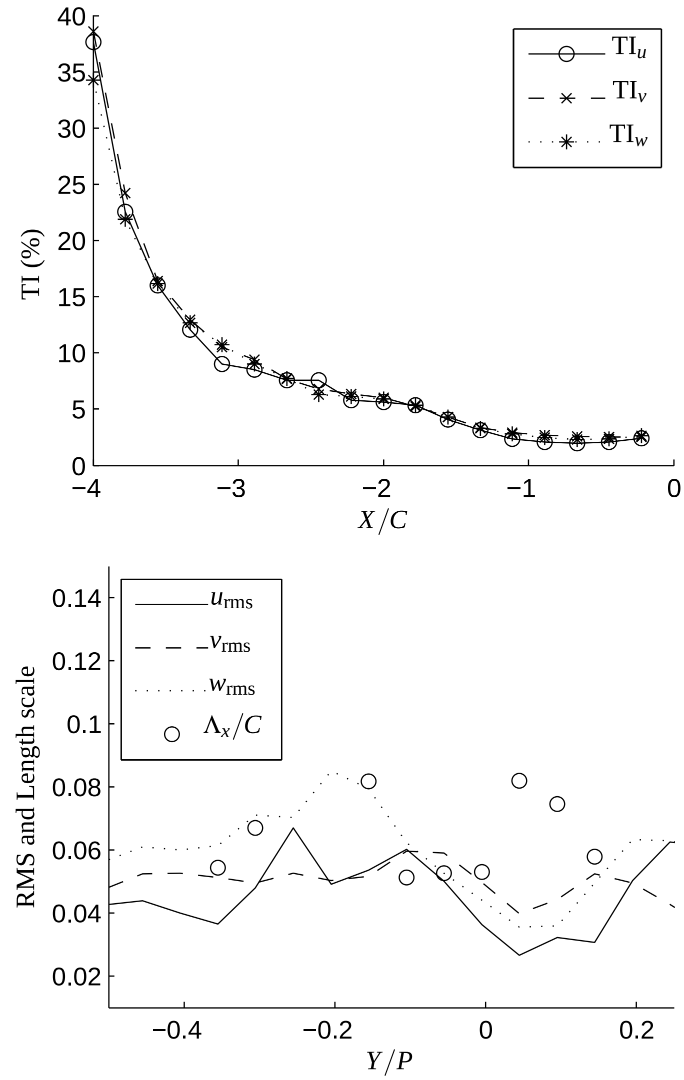


**FIGURE 13**. Decay of fluctuating components of velocity from turbulence generating grid to cascade leading edge($X/C=0.0$) for the baseline DNS. A nearly isotropic turbulence is achieved just upstream of the stagnation region. Achieving higher, engine-like TI (8-20 %) is achievable at higher Reynolds numbers.

scribed in the previous section, a sustained turbulence intensity of 2.1% is achieved just upstream of the blade. At a Reynolds number closer to engine conditions, less dissipation in the inflow section would result in a higher TI.

### 3.2 Vortex dynamics

A vector plot in combination with velocity contour lines is shown in Fig. 14 (top-left). Several leading edge horseshoe vortices which were not observable in the experiments are found, where the most intense vortex one is located nearest to the vane. It is strong enough to accelerate free stream fluid towards the endwall and against the main flow. The incoming flow does not have enough momentum to suppress the formation of secondary leading edge vortices. Multiple vortices are also evident in the plot of turbulent kinetic energy (Fig.14) that shows one circular shaped region of high levels close to the vane and smaller ones further upstream. The overall level of turbulent kinetic energy is lower than what was shown in Radomsky et al. (2000) [9] and the vortex location is shifted further upstream. The cooling-hole case

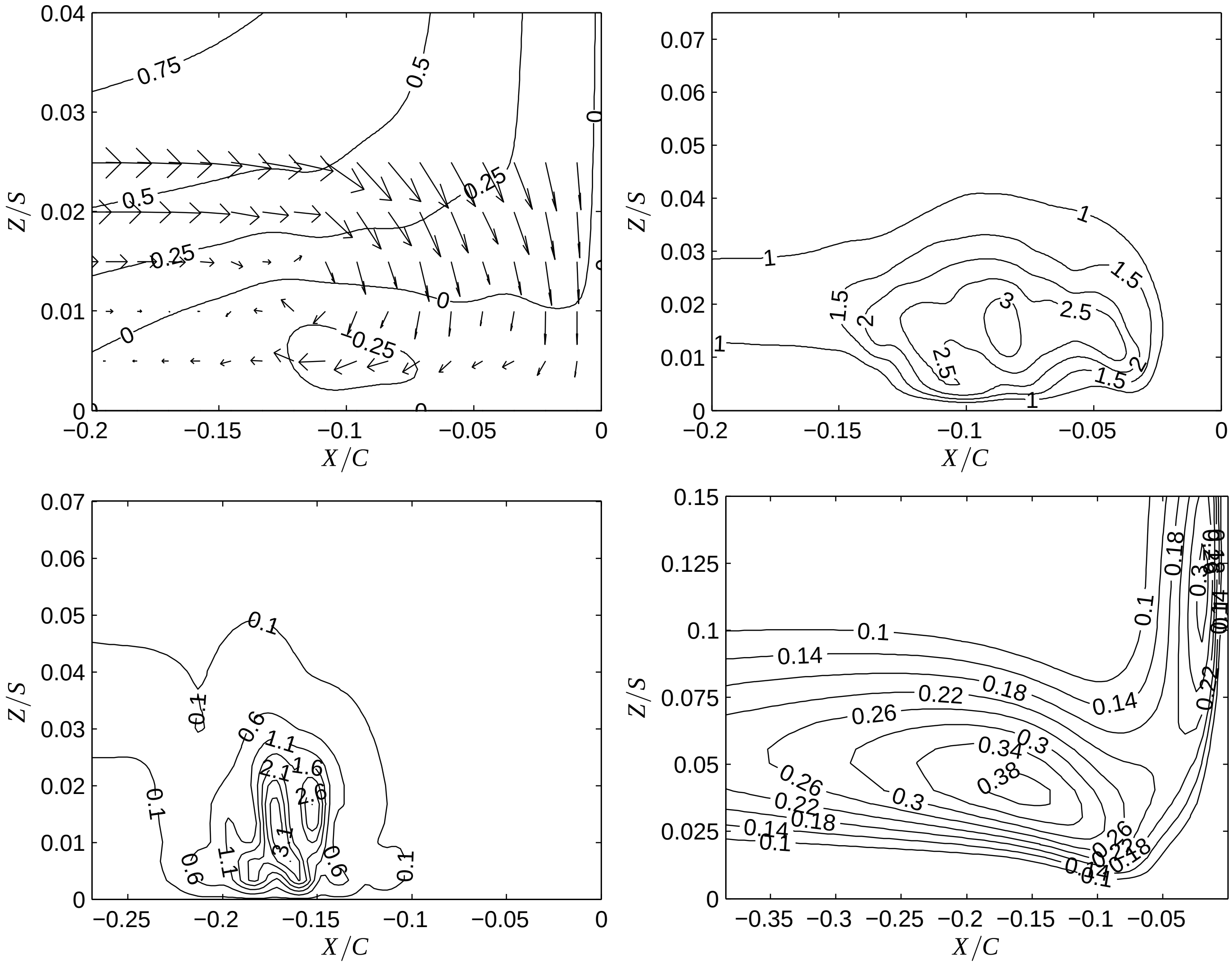


**FIGURE 14**. (Top-left) Contours and vectors of average velocity on the stagnation plane for the baseline DNS. The average effect of the vortex is seen near $X/C$=-0.1. Contours of turbulent kinetic energy, scaled by 100, from DNS (top-right), cooling hole DNS (bottom-left), and LES (bottom-right). The horseshoe vortex from the baseline DNS appears to have two main regions of activity, up and downstream of $X/C = -0.07$. The LES model dissipates too much turbulence during the large strain region and does not capture the structure of the vortex. The cooling-hole DNS exhibits a shift upstream as well as evidence of multiple vortex cores.

exhibits multiple vortex cores, shown in Fig.14 (bottom-left).

Higher experimental Reynolds number may be attributed to the observed differences, however at higher Re one would expect the number of unique vortices to increase. The interaction between these vortices may be an important reason why the endwall heat transfer is significantly augmented.

Comparing the performance of the LES model the reported values of turbulent kinetic energy for the LES are much lower than the DNS. Examining the turbulent intensity in Fig. 14 (bottom-right) shows that the HPF model may be removing key turbulent structures as the vortex structure is not captured. For the LES model, the eddy viscosity term was added into the normal viscosity to multiply with the full strain rate tensor as in classical LES approaches: $\tau_{\text{SGS}} = \nu_t S_{ij}$. However, because this stator flow has large anisotropy from regions of high acceleration, such as the ramp, entrance length, and turbine vane passage, the large strain rate may be damping the turbulence and skewing the results. This is also evident in the velocity profiles for the LES where the profiles appear to be laminar, in Fig.12. A possible correction to this issue would be to use the filtered strain rate with the eddy viscosity term: $\tau_{\text{SGS}} = \nu_t S_{ij}(\tilde{u})$.

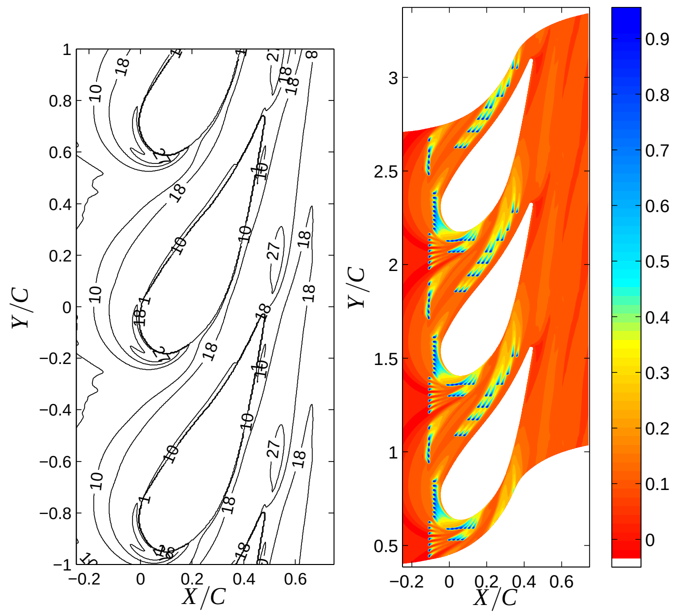


**FIGURE 15**. Contours of Stanton number from the non-cooling hole DNS case, scaled by 100 (left), and cooling-hole DNS case adiabatic effectiveness (right). These compare qualitatively well to experimental data from Kang et al. (1999) [7], although accuracy is not expected due to the large difference is Reynolds number.

### 3.3 Heat transfer

Heat transfer on the endwall is shown in Fig. 15. The highest regions of heat transfer for the no cooling hole case is upstream of the stagnation point due to the leading edge horse shoe vortex, and in the wake of the blade. A region of lower heat transfer (isoline 9) extends from the inflow section into the first third of the passage. In this area no secondary flow increases mixing and the boundary layer is being accelerated. Approaching the trailing edge of the passage, areas of elevated heat transfer are shifted towards the vane suction side, following the trace of the passage vortex (see isolines 13 and 18). This same shift can be seen in the plot of adiabatic effectiveness, where the trace of the downstream cooling holes bends towards the suction surface.

The interaction between secondary flow structures and endwall temperature is further visualized in Fig. 16. Isosurfaces of coherent vorticity for the smooth case and the cooling hole domain show multiple leading edge vortices that merge through the passage and decrease wall temperature. The isosurface of the cooling hole case is at a different level of coherent vorticity and also taken from a fairly early time step, where the incoming flow is still developing.

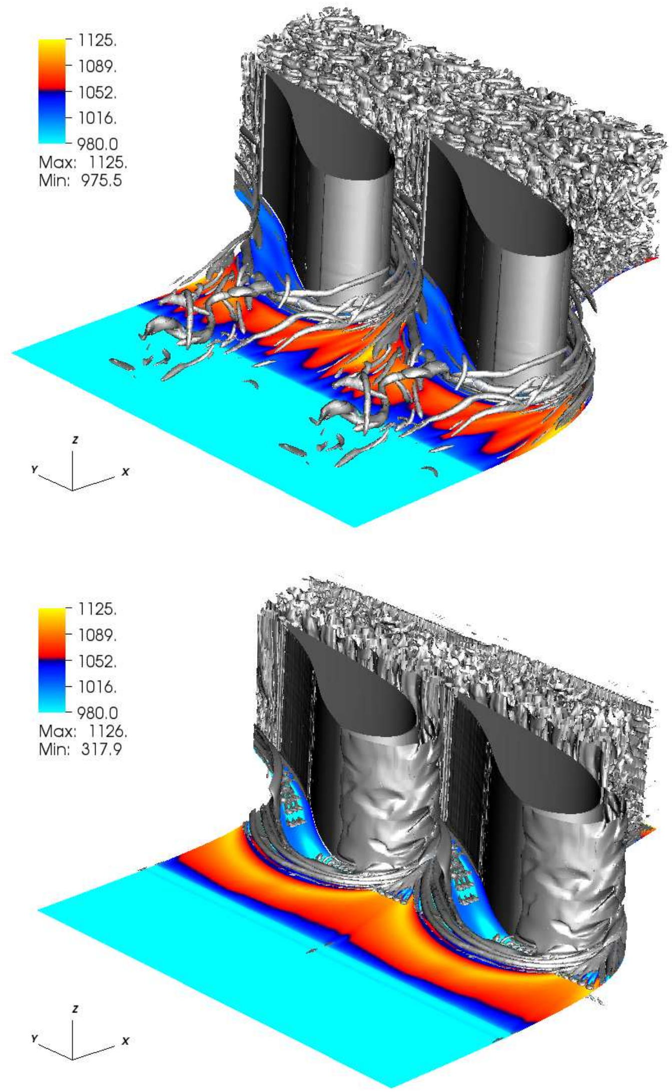


**FIGURE 16**. Isosurfaces of coherent vorticity (grey) and endwall temperature contours of the baseline (top) and cooling holes (bottom) DNS. In both cases, the effect of the horseshoe vortex is dominant on endwall temperature. The cooling hole case qualitatively exhibits more vortex cores at the stagnation region.

## 4 Conclusions

Simulation of a high-pressure first stage turbine for a less than engine-condition Re=10,000 were performed to examine the dynamics of the stagnating horseshoe vortex on endwall heat transfer. At this Reynolds number, the vortex still exhibits strong aperiodic motions which are responsible for the heat transfer augmentation and using DNS instead of LES can avoid errors in the physics due to LES turbulence modeling. This error was evident when using a high-pass-filtered Smagorinsky model which was unable to resolve the vortex dynamics on a coarser grid. Although this model should perform better in regions of high freestream acceleration, the turbulence intensity in the freestream was damped out resulting in very different dynamics.

The direct numerical simulations with and without cooling holes are the first time-resolved computational investigation of the horseshoe vortex. For the baseline case with no cooling holes, the vortex appears to have a bi-modal distribution. The presence of cooling holes appears to increase the number of vortex cores present, resulting in more complex dynamics. There was good general qualitative agreement for the cooling-hole simulation to that of the experimental data, although accuracy is not expected with such a large difference in Reynolds number. Further analysis of the time-dependent data will continue to characterize the horseshoe vortex dynamics and its effect on endwall heat transfer.

## ACKNOWLEDGMENT

The authors acknowledge the Texas A&M Supercomputing Facility and NSF Teragrid for providing computing resources that were essential in the research reported in this paper. Fruitful interactions with Karen Thole and Paul Fischer are gratefully acknowledged.

## REFERENCES

[1] Langston, L. S., 2001. “Secondary flows in axial turbines - a review”. *Ann. New York Acad. Sci.,* ***934***, pp. 11–26.

[2] Thole, K., 2008. personal communication.

[3] Saha, A. K., and Acharya, S., 2008. “Computations of turbulent flow and heat transfer through a three- dimensional nonaxisymmetric blade passage”. *J. Turbomachinery,* ***130***, pp. 031008–1–10.

[4] Lynch, S. P., Sundaram, N., Thole, K. A., Kholi, A., and Lehane, C., 2009. “Heat transfer for a turbine blade with non-axisymmetric endwall contouring”. *ASME Paper GT2009-60185*.

[5] Denton, J., 2010. On the use of CFD in turbine design. “Axial flow turbines - key technologies to come.” Turbomachinery: Axial Flow Turbine Aerodynamics panel session, ASME IGTI 2010.

[6] Gaugler, R. E., and Russell, L. M., 1984. “Comparison of visualized turbine endwall secondary flows and measured heat transfer patters”. *ASME J. Eng. Gas Turbine Power,* ***106***, pp. 168–172.

[7] Kang, M., Kohli, A., and Thole, K. A., 1999. “Heat transfer and flowfield measurements in the leading edge region of a stator vane endwall”. *J. Turbomachinery,* ***121***, pp. 558–568.

[8] Devenport, W. J., and Simpson, R. L., 1990. “Time-dependent and time-averaged turbulence structure near the nose of a wing-body junction”. *J. Fluid Mech.,* ***210***, pp. 23–55.

[9] Radomsky, R., and Thole, K. A., 2000. “High freestream turbulence effects in the endwall leading edge region”. *J. Turbomachinery,* ***122***, pp. 699–708.

[10] Knost, D. G., Thole, K. A., and Duggleby, A., 2009. “Evaluating a slot design for the combustor-turbine interface”. *ASME Paper GT2009-60168*.

[11] Gregory-Smith, D. G., and Cleak, J. G. E., 1992. “Secondary flow measurements in a turbine cascade with high inlet turbulence”. *Journal of Turbomachinery,* ***114***(1), pp. 173–183.

[12] Spencer, M. C., Jones, T. V., and Lock, G. D., 1996. “Endwall heat transfer measurements in an annular cascade of nozzle guide vanes at engine representative Reynolds and Mach numbers”. *International Journal of Heat and Fluid Flow,* ***17***(2), pp. 139 – 147.

[13] Knost, D. G., and Thole, K. A., 2005. “Computational predictions of endwall film-cooling for a first stage vane”. *International J. of Turbo and Jet Engines,* ***22***, pp. 41–58.

[14] Knost, D. G., and Thole, K. A., 2005. “Adiabatic Effectiveness Measurements of Endwall Film-Cooling for a First Stage Vane”. *J. of Turbomachinery,* ***127***, pp. 297–305.

[15] Fischer, P. F., Lottes, J. W., Pointer, D., and Siegel, A., 2008. “Petascale algorithms for reactor hydrodynamics”. In SciDac08.

[16] Fischer, P. F., Ho, L. W., Karniadakis, G. E., Ronouist, E. M., and Patera, A. T., 1988. “Recent advances in parallel spectral element simulation of unsteady incompressible flows”. *Comput. & Struct.,* ***30***, pp. 217–231.

[17] Lottes, J. W., and Fischer, P. F., 2004. “Hybrid multigrid/Schwarz algorithms for the spectral element method”. *J. Sci. Comp.,* ***24***(1), pp. 45–78.

[18] Tufo, H. M., and Fischer, P. F., 1999. “Terascale spectral element algorithms and implementations”. In Proc. of the ACM/IEEE SC99 Conf. on High Performance Networking and Computing, IEEE Computer Soc. Gordon Bell Prize paper.

[19] Fischer, P. F., and Lottes, J. W., 2003. “Hybrid Schwarz-multigrid methods for the spectral element method: Extensions to Navier-Stokes”. In Proc. of the 15th Int. Conf. on Domain Decomposition Methods.

[20] Duggleby, A., and Paul, M., 2010. “Computing the Karhunen-Loève dimension of an extensively chaotic flow field given a finite amount of data”. *Computers & Fluids,* ***39***, pp. 1704–1710.

[21] Duggleby, A., Ball, K. S., and Schwaenen, M., 2009. “Structure and dynamics of low reynolds number turbulent pipe flow”. *Phil. Trans. Roy. Soc. A,* ***347***, pp. 473–488.

[22] Duggleby, A., Ball, K. S., Paul, M. R., and Fischer, P. F.,

2007. “Dynamical eigenfunction decomposition of turbulent pipe flow”. *J. of Turbulence*, ***8***(43), pp. 1–24.
[23] S. Kerkemeier, S. Parker, P. F. F., 2010. Scalability of the NEK5000 spectral element code. Jülich Blue Gene/P Extreme Scaling Workshop 2010, technical report.
[24] Blacker, T. D., Stephenson, M. B., and Canaan, S., 1991. “Analysis automation with paving - a new quadrilateral meshing technique”. *Advances in Engineering Software and Workstations*, ***13.5-6***, pp. 332–337.
[25] Stolz, S., 2005. “High-pass filtered eddy-viscosity models for large-eddy simulations of compressible wall-bounded flows”. *Journal of Fluids Engineering*, ***127***(4), pp. 666–673.
[26] Stolz, S., and Adams, N. A., 2003. “Large-eddy simulation of high-reynolds-number supersonic boundary layers using the approximate deconvolution model and a rescaling and recycling technique”. *Physics of Fluids*, ***15***(8), pp. 2398–2412.
[27] Paul Fischer, J. M., 2001. “Filter-based stabilization of spectral element methods”. *C.R.Acad. Sci. Ser. I-Anal Numer.*, ***163***, pp. 193–204.
[28] Fischer, P. F., Kruse, G. W., and Loth, F., 2002. “Spectral element methods for transitional flows in complex geometries”. *J. Sci. Comput.*, ***17***(1-4), pp. 81–98.